# Energy and Technology Review

Lawrence Livermore National Laboratory

October 1988

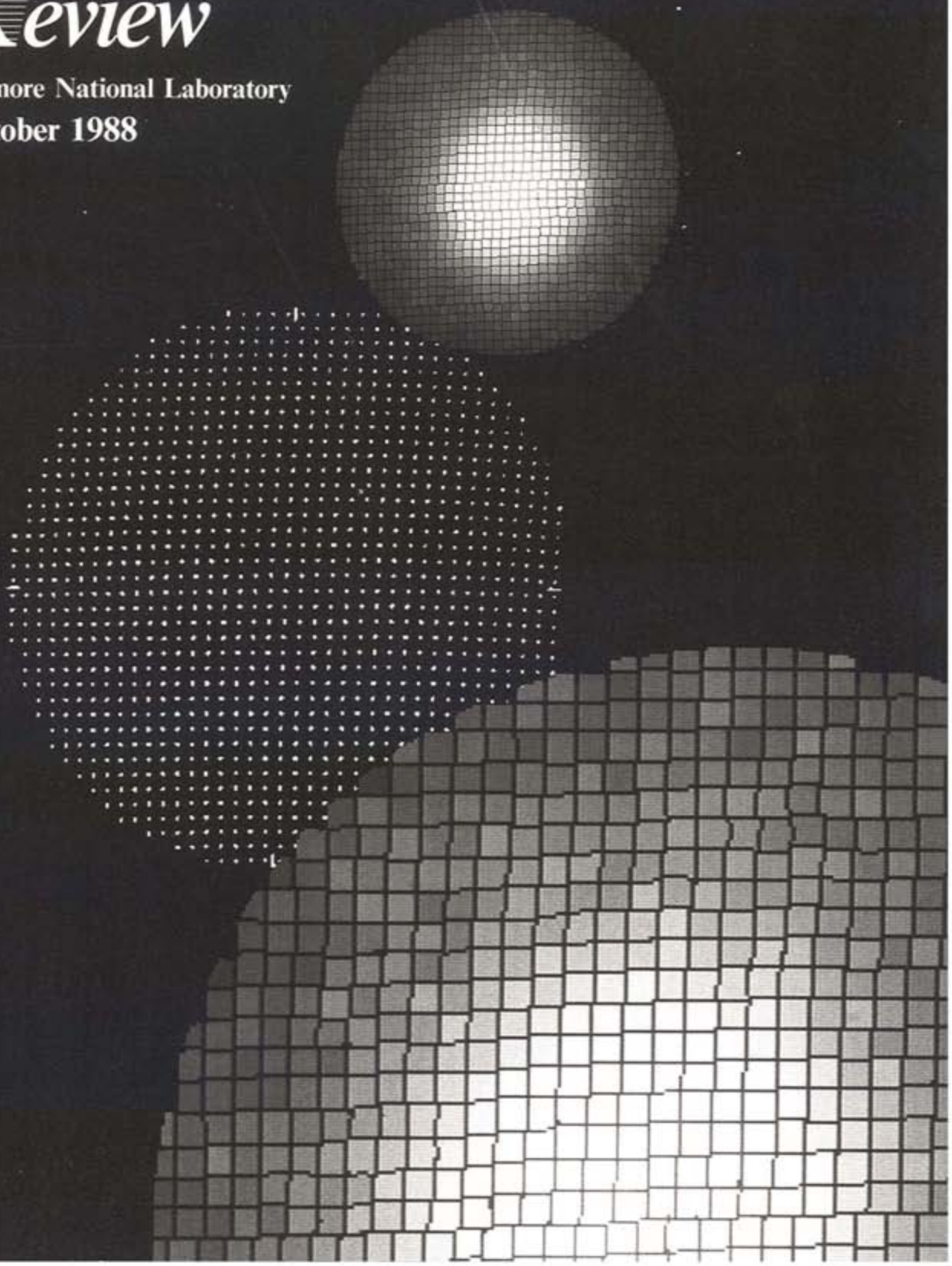

# Neutron Penumbral Imaging of Laser-Fusion Targets

***Using a new technique, penumbral coded-aperture imaging, we have obtained the first neutron images of laser-driven, inertial confinement fusion targets. With these images we can measure directly the deuterium-tritium burn region within a compressed target.***

*For further information contact Richard A. Lerche (415) 422-5364 or David B. Ress (415) 423-8195.*

A long-term goal of LLNL's Inertial Confinement Fusion Program is to demonstrate that electric power can be produced by imploding targets containing deuterium-tritium (D-T) fuel. Our expectation is that such power can be made commercially competitive with power from other sources.

Efficient energy production requires that inertial confinement fusion (ICF) targets produce about 100 times more energy than is used to drive the implosion. Such high gain can be achieved by using laser energy to compress the fuel. Most of the fuel is compressed to a density of a few hundred grams per cubic centimeter at a relatively low ion temperature ($\sim$1 keV). At the center of the highly compressed fuel is a small "hot spot" containing about 1% of the fuel mass at a much lower density (on the order of 30 g/cm$^3$) but higher ion temperature ($\sim$4 keV). Fusion starts in this central hot spot with the release of energetic neutrons and alpha particles. The reaction advances into the surrounding, highly compressed fuel via a spherical, thermonuclear burn wave that propagates by energy transfer from the alpha particles to the D-T plasma.

We use images of the burning fuel to verify calculations of the implosion physics and to determine the existence of asymmetries. However, viewing a target with sufficient resolution is extremely difficult, and previous methods have not been completely satisfactory. For example, x-ray emission, which is the basis for many widely used ICF diagnostic instruments, depends on the spatial and temporal profiles of plasma density, ionization state, and electron temperature. During an ICF implosion, ion and electron temperatures can be quite different, and mixing of target components leads to complicated spatial variations in the ionization state. Thus, an x-ray image provides information about the spatial structure of several complex processes within the target that are not directly related to hot-spot formation, fuel ignition, or the fusion reaction.

A neutron image, on the other hand, provides a direct measurement of the spatial extent of fusion reactions. Furthermore, in targets that achieve high compression, most reaction products and x rays are absorbed within the target while the penetrating neutrons escape unperturbed. It is for this reason that neutron imaging has long been recognized for its potential to diagnose unambiguously both compression and hot-spot formation in burning fuel.[1]

Many of our future ICF experiments with our Nova laser will focus on the physics of hot-spot formation, and we will require measurement techniques such as neutron imaging. Relevant implosions will produce neutron emission from regions 20 $\mu$m in diameter with yields of $10^{11}$ neutrons per implosion. Conventional pinhole imaging is not sensitive enough to produce neutron images of such targets; even with a larger neutron yield, the techniques for fabricating the required pinhole are not yet developed. Penumbral imaging, a technique recently developed to obtain x-ray images of laser-produced plasmas,[2] is a much more efficient method of imaging neutrons emitted by ICF targets.

Our recent numerical and theoretical calculations verified the feasibility of neutron penumbral imaging. We have now built a system specifically designed to demonstrate the technique of neutron penumbral imaging, and we have obtained excellent experimental results with our preliminary system.[3]

## Penumbral Imaging

Penumbral imaging is a two-step technique involving coded-aperture imaging. Coded-image formation (Figure 1) is similar to pinhole imaging but with the essential difference that the aperture is larger than the size of the source. In the first step, a source of incoherent radiation casts a geometrical shadow through a circular aperture, thereby producing a coded image that consists of a bright, uniformly illuminated central region surrounded by a partially illuminated penumbra. All of the information about the spatial distribution of a source is encoded in the penumbra.

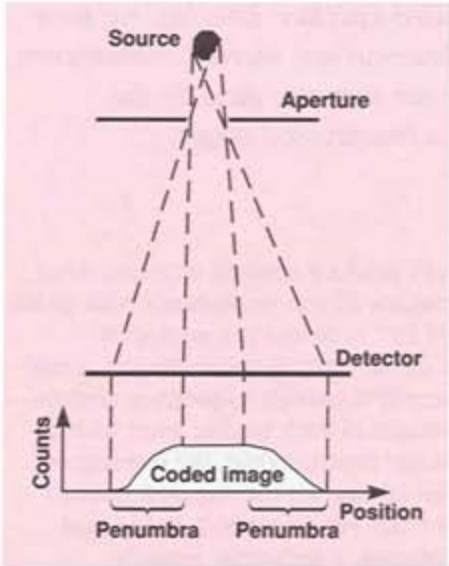


**Figure 1.** Concept of penumbral imaging. A source casts a geometrical shadow through a circular aperture to produce a coded image. The penumbra of the coded image contains information about the shape of the source. The scale of this figure differs from that for our experimental system, but the principle of operation is the same.

However, because the coded image is the convolution of the source distribution with the aperture transmission function, it does not represent the actual appearance of the source itself. In the second step, the source distribution is deconvolved (i.e., extracted by mathematical techniques) from the coded image. In other words, we decode the image to determine the shape of the original source using numerical techniques and knowledge of the aperture shape.

## Aperture Design

To obtain an image of the highly penetrating, 14-MeV D-T fusion neutrons with the technique of penumbral imaging, the aperture must be thick enough to provide sufficient image contrast; it should also be specially tapered to provide a sharp point-spread function that is invariant with the position of a source (that is, isoplanatic). To provide the necessary contrast, we fabricated our aperture from a gold cylinder. Many of the neutrons are not stopped by the gold but instead are scattered with a mean free path of 3.2 cm. Because our aperture is located quite far from the detector, virtually none of the scattered neutrons is detected.

A particularly satisfactory taper for our aperture is a toroidal segment (Figure 2a) with a radius of curvature $R$ (minor radius of the toroid) much greater than the aperture thickness $t$. The principle of the toroidal taper is that rays drawn from various positions in a source plane produce similar cutoffs as they are moved from the edge of the aperture into the torus. Some distortion is introduced because magnification depends on the position of the source point. Our aperture can be regarded as formed from a segment of a toroidal solid; by proper choice of the segment, we can minimize distortion.

**Figure 2.** (a) Principle of the toroidal segment aperture. To obtain an image of penetrating radiation, the aperture must be thick enough to provide sufficient image contrast and be specially tapered to provide an isoplanatic point-spread function. A particularly satisfactory taper is a toroid with a radius of curvature much greater than the aperture thickness. A practical realization of this concept uses a segment of the toroid.
(b) Aperture used in our neutron imaging experiments.

(a)

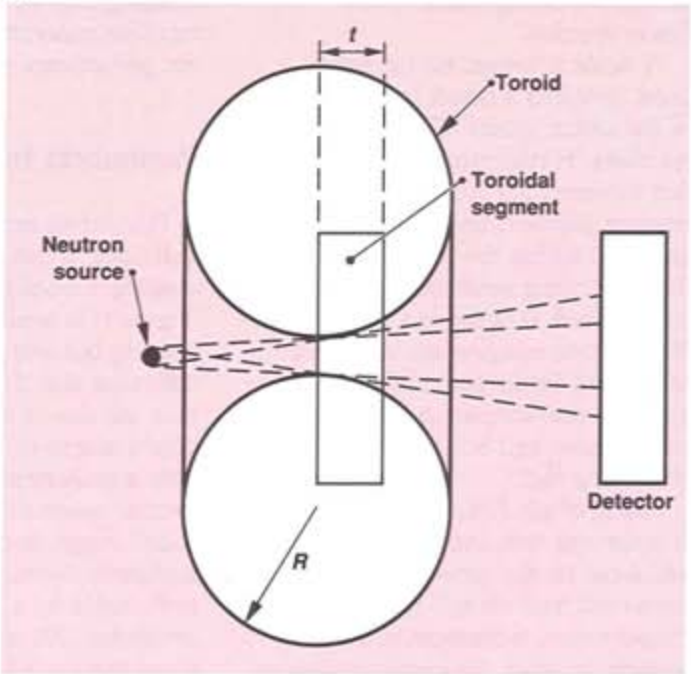


(b)

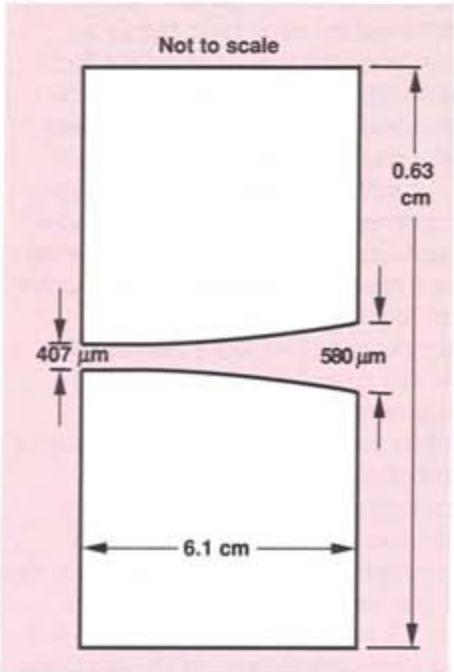

Aperture design is a process of compromise because the optimum dimensions depend on maximum size of the source, source-to-aperture distance, aperture material, and required resolution. The larger the aperture radius of curvature, the sharper the cutoff but the less isoplanatic the response.

We obtained the images that are presented subsequently in this article with the aperture shown in Figure 2b. We made this aperture along the axis of a gold cylinder 0.63 cm in diameter and 6.1 cm long, with a minimum diameter of 407 $\mu$m and a radius of curvature of 19.5 m. For this design, the magnification varies by $\pm 3\%$ across the field of view of 400 $\mu$m, while the 10%-to-90% width of the cutoff is 30 $\mu$m referred to the source plane.

Fabrication of our aperture was greatly simplified, compared to the process required for constructing a pinhole aperture, because the diameter of the opening was large compared to the desired resolution. We fabricated our aperture using an electroforming technique in which gold is electroplated onto a precisely formed brass mandrel. The brass core is then etched out of the gold cylinder to form the aperture itself. Numerical image reconstruction requires precise knowledge of the neutron aperture point-spread function; such information is obtained by careful mechanical characterization of the brass mandrel during fabrication.

## Aperture Alignment

Precise alignment of an aperture to the ICF target is critical to our imaging system. The axis of the aperture, which was located 15 cm from the target, had to be pointed to within 50 $\mu$m of target center to keep the source within the system's field of view. In addition, the detector, which was located 10.5 m from the target, had to be centered on the axis of the aperture with an accuracy of a few millimeters. We developed a relatively simple technique that allows both rapid and accurate alignment.

Our alignment technique (Figure 3) takes advantage of the properties of coherent light and spherical aberration to form a pair of ring-shaped interference patterns. A slowly converging laser beam illuminates a 2-mm-diameter glass ball positioned at the center of the target chamber. The ball expands the beam and introduces spherical aberration. Plano-convex lenses that are optically centered on each end of the aperture independently cause portions of the beam to slowly converge in a region outside the target chamber. The convex side of the second lens is ground and polished flat over its central region to allow light from the first lens to pass through without effect.

Slowly converging, severely aberrated beams create a long region of interference so that the ring patterns overlap to form a moiré pattern. For our application, the ring patterns were visible over the entire

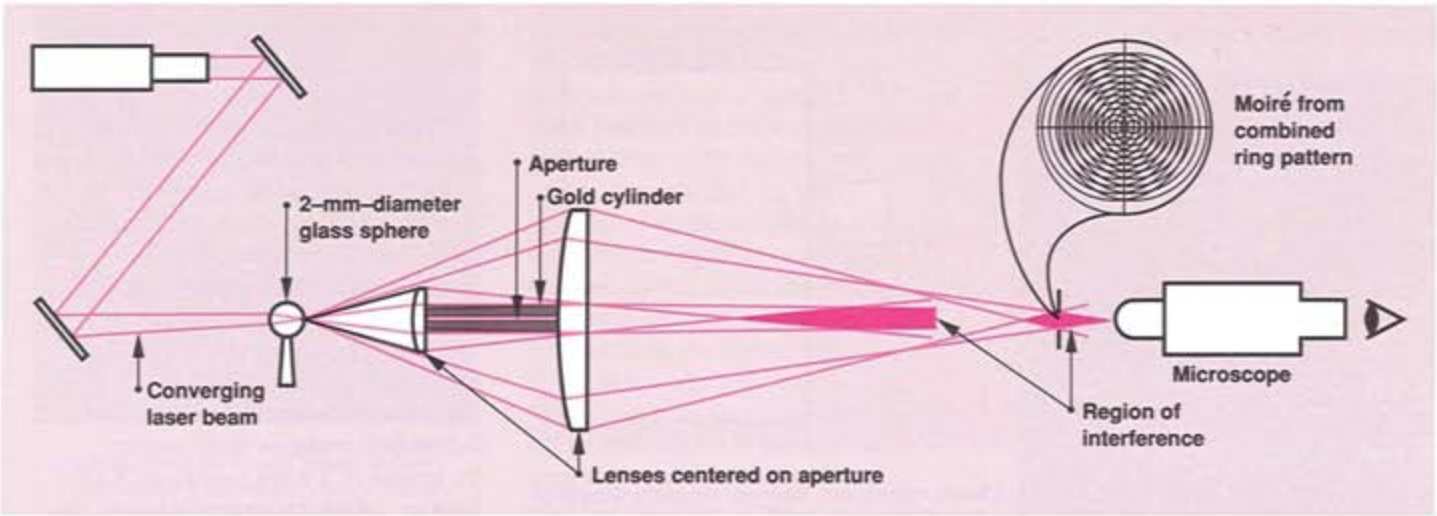


**Figure 3.** Alignment technique. A 15-mW helium-neon laser located 4.5 m from the 2-mm-diameter glass alignment ball is expanded to a 25-mm diameter and steered with a pair of mirrors. The moiré pattern is viewed through a 50 × microscope attenuated with an optical density of 3.0. The microscope is just outside the target chamber and 2.4 m from the glass sphere. The detector (not shown) is located within the region of interference, 10.5 m from the glass sphere.

10.5-m line of sight of the instrument. Figure 4 shows moiré patterns formed 2.4 m from the target and viewed through the alignment microscope. We mechanically adjust the aperture alignment until the ring patterns are concentric. At this point, the aperture axis is pointed at the center of the alignment ball with the required accuracy. The detector is then centered on the ring pattern to complete the alignment process.

## Detector System

The number of neutrons available to form a coded image is relatively small for the targets that are of interest to us. Thus, a primary consideration for choosing a detector system for our imaging experiments was its efficiency for detecting 14-MeV neutrons. The detector system shown in Figure 5 consists of four principal components: a scintillator array, a fiber-optic minifier, an image intensifier, and a charge-coupled-device (CCD) camera.

The heart of the detector system is an 8-cm-diameter circular array of 1240 plastic elements. Each element is a 10-cm-long rod with a square cross section 2 mm on a side. The plastic scintillator material converts the deposited neutron energy to blue light. Within the scintillator, neutrons interact primarily through elastic scattering events with hydrogen nuclei to produce recoil protons that excite the scintillator as they slow down. The cross section of each detector element is matched to the 0.7-mm maximum transverse range of these recoil protons. On average, about 25% of the incident neutron energy is deposited in each element, and blue light is produced in proportion to the amount of energy deposited.

In addition to detecting neutrons, each scintillator element acts as a light guide to transport scintillator light to the output surface of the array. The 10-cm-long sides of each scintillator achieve total internal reflection via a polished scintillator-air interface. Thin paper spacers at each end of a scintillator element separate it from adjacent elements with an air gap.

Because the blue light from our scintillator is too faint for direct recording, it must be amplified. We coupled the 8-cm-diameter scintillator image to a 4-cm-diameter microchannel-plate image intensifier with a 2:1 coherent fiber-optic minifier. The image intensifier provides a luminous gain of approximately ten thousand. The intensified image is then coupled by means of a relay lens to a CCD camera, which temporarily stores the image and converts it to digital form. Digital information is transferred to magnetic storage media with an LSI-11 computer. Figure 6 shows a coded image recorded in this fashion.

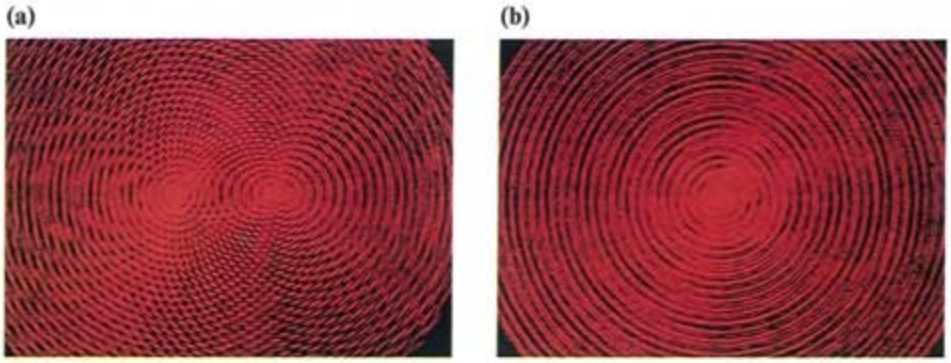


**Figure 4.** Moiré patterns formed by the interference of two ring patterns viewed through the alignment microscope. (a) Aperture axis pointing error at the target equal to 126 $\mu$m. (b) Aperture axis correctly aligned to the center of the alignment sphere.

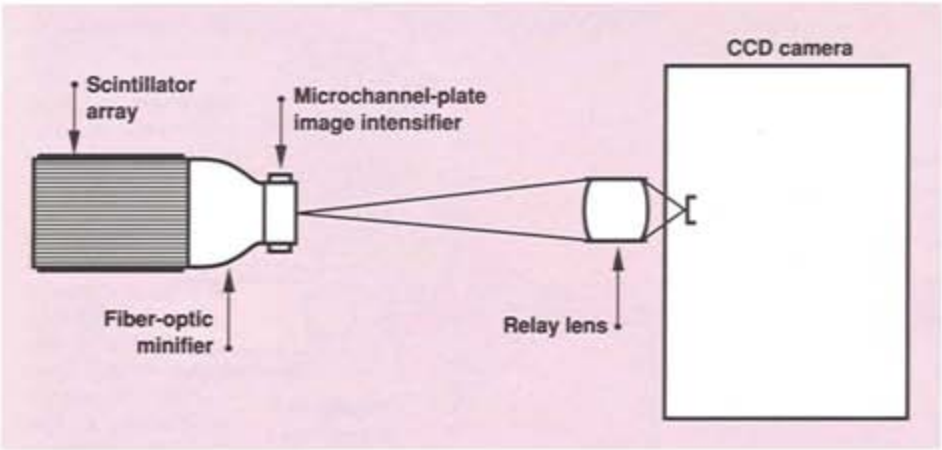


**Figure 5.** Schematic of the detector system. Plastic scintillator material converts deposited neutron energy to blue light. Because the blue light from our scintillator is too faint for direct recording, it must be amplified. The 8-cm-diameter scintillator image is coupled to a 4-cm-diameter microchannel-plate image intensifier with a 2:1 fiber-optic minifier. The image intensifier provides a luminous gain of approximately ten thousand. The intensified image is then coupled by means of a relay lens (0.22 × magnification) to a CCD camera, which temporarily stores the image and converts it to digital form.

## Image Reconstruction

As described previously, our recorded image is coded and does not represent the actual appearance of the original source. To obtain a useful image of the source, we must remove from the coded image the distortion caused by our imaging system and deconvolve the effect of the aperture point-spread function.

Characteristics of the imaging system that distort the recorded image include:

- CCD camera offset and fixed-pattern background noise.
- Random dots (salt-and-pepper noise) caused by neutrons traveling through the plastic scintillator and interacting directly in the CCD.
- Uniform background outside the image area caused by neutrons passing directly through the gold that forms the aperture.
- CCD-to-scintillator pixel mapping. (The image is recorded with a 384 × 576-element CCD array; however, the fundamental resolution in a recorded image is limited by each of the 1240 scintillator elements. Thus, we must map each CCD element to its corresponding scintillator element.)
- Spatial variations in detector sensitivity.
- Geometrical distortion introduced by the fiber-optic minifier.
- Nonuniform spacing of scintillator elements.

We must remove such instrumental effects from a recorded image before deconvolving the effect of the aperture point-spread function. First, we subtract the fixed-pattern background by using an image recorded during a background test when no neutrons are present. For our images, the number of noise spikes is low relative to the total number of CCD pixels. Each spike extends over only a few pixels, which are easily identified by their large signal relative to the surrounding area.

Because approximately 80 CCD elements record light from each scintillator element, we must generate a one-time CCD-to-scintillator pixel map. We create the map by removing the light-tight front cover of the detector and illuminating the front of the scintillator array with light from a distant source. In the resulting image, CCD elements that lie along scintillator element boundaries have a 5% dip in signal because light is blocked by the paper spacers. We find the signal for each scintillator element by summing the signals recorded in the corresponding CCD elements.

We measure the spatial sensitivity of the detector by exposing the detector to a temporally short, spatially uniform burst of neutrons. We use high-yield shots generating $10^{13}$ neutrons at Nova with the detector placed 2.5 m from the target and with no aperture in place. From the resulting image, we determine the relative sensitivity for each scintillator element. Each coded image is corrected (or "flat-fielded") for this sensitivity variation. Figure 7 shows the image in Figure 6 after spike removal, CCD-to-scintillator pixel mapping, and flat-fielding.

The fiber-optic minifier introduces noticable geometrical distortion into the image. Figure 8 shows the image

**Figure 6. Neutron coded image before reconstruction. Distortions caused by the imaging system that are observable in this image include neutron spikes, uniform background, spatial variation in detector intensity, and nonuniform scintillator-element spacing. This image was recorded for a high-yield target that produced $1.2 \times 10^{13}$ neutrons.**

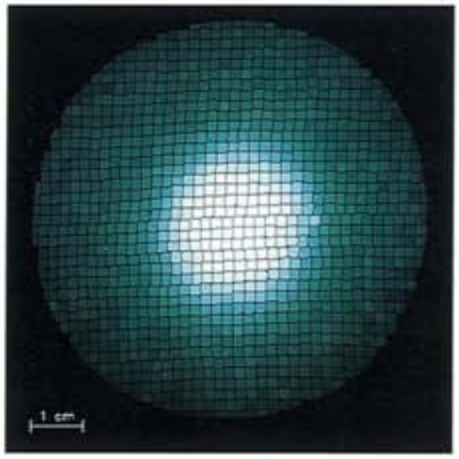


**Figure 7. Partially corrected coded image. Shown here is the image in Figure 6 after neutron spike removal, CCD-to-scintillator mapping, and correction.**

**Figure 8. Enhanced image of grid pattern. We used this image of a mask with pin-holes located 2 mm apart on a uniformly spaced grid to quantify geometrical distortion in the detector system.**

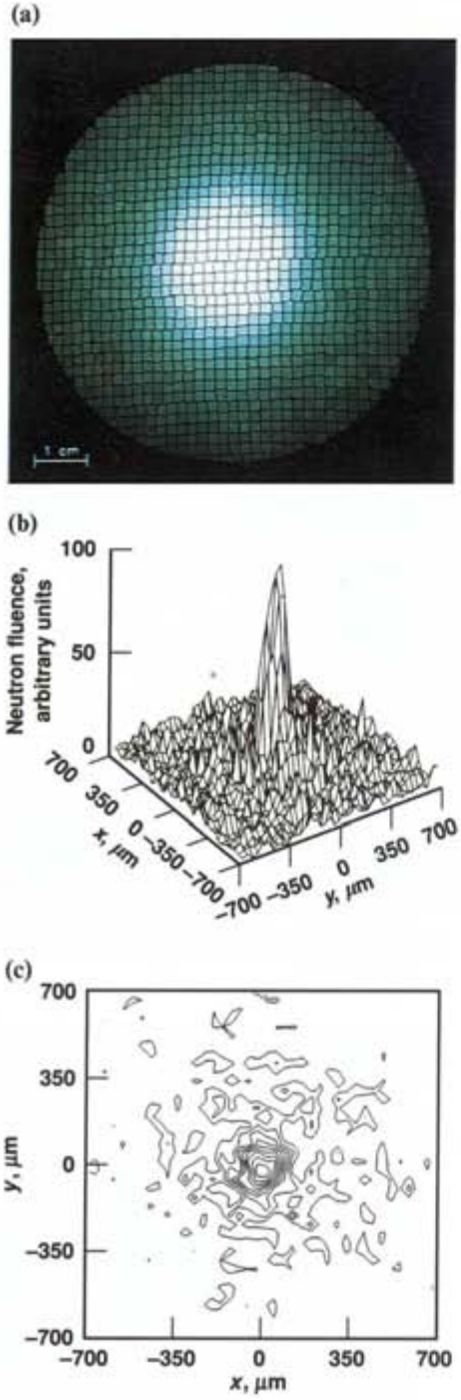


**Figure 9.** Neutron image recorded for a typical high-yield target ($10^{13}$ neutrons). (a) Coded image. (b) Isometric representation of the reconstructed neutron source. (c) Contour plot of (b) looking downward on the *x-y* plane.

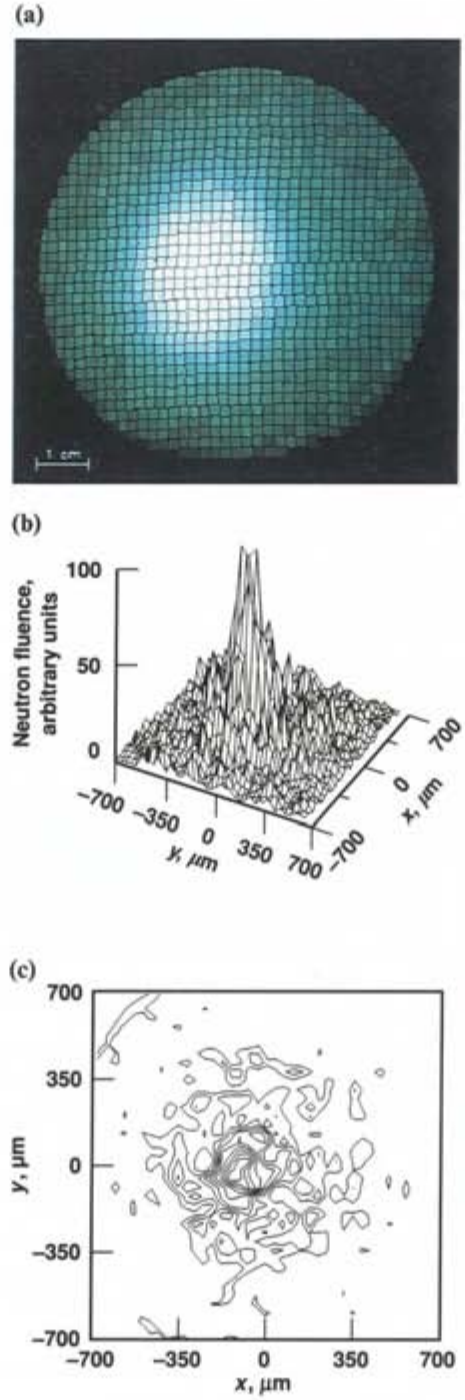


**Figure 10.** Neutron image recorded for a high-yield target ($3 \times 10^{12}$ neutrons) intentionally heated with nonuniform laser light. (a) Coded image. (b) Isometric representation of the reconstructed neutron source. (c) Contour plot of (b) looking downward on the *x-y* plane.

of a mask with pinholes located 2 mm apart on a uniformly spaced grid. The mask is placed in contact with the minifier and illuminated. We use bilinear interpolation to determine the true position of each scintillator element relative to the CCD pixels.

Our deconvolution technique requires the coded image to be comprised of an array of values at uniformly spaced coordinates. Because the scintillator array has nonuniform spacing, we use an additional interpolation step to convert the irregularly spaced data to regularly spaced data.

Recall that our recorded coded image is the convolution of the neutron source distribution and the aperture point-spread function. The effect of the aperture on the coded image must be deconvolved to obtain a neutron source distribution. In penumbral imaging, the Fourier transform of the point-spread function has a central lobe that is much narrower than that of the source, and the side lobes are separated by zeros that extend to higher frequencies. Spatial frequency components that lie close to these zeros have a poor signal-to-noise ratio and must be deemphasized during the deconvolution process. We use a parametric Wiener filter for this purpose. The Wiener filter does not cause distortion of the image but does introduce some low-pass filtering (or blurring). For neutron images from Nova, the loss of resolution is quite small, approximately 15%.

## Neutron Images

The neutron images we recorded during recent experiments at Nova illustrate the capabilities of our new imaging diagnostic. The ICF targets were spherical glass shells 1 mm in

diameter with walls 2 $\mu$m thick; these were filled with 2.5 MPa (25 atm) of equimolar D-T gas. To achieve an implosion, a target is irradiated directly with the Nova laser. The laser consists of two five-beam clusters that produce a complex, asymmetric illumination pattern on the target. More than 20 kJ of 351-nm light is focused onto the target in a 1-ns temporally square pulse. Unlike the optimal target designs discussed previously, these targets do not produce strong fuel compression; instead they generate large neutron yields by achieving a high ion temperature (9 keV). Radial convergence of the glass shell is less than three, thus producing a relatively large neutron-source region compatible with the resolution of our imaging system. Neutron yields varied from $2.0 \times 10^{12}$ to $1.2 \times 10^{13}$, and the duration of the fusion burn was measured with photoconductive devices to be in the range 300–400 ps full width at half maximum (FWHM).[4]

We have obtained images for our high-yield, directly illuminated targets that produce a typical yield of $10^{13}$ neutrons. Figure 9a is a representative coded neutron image with approximately 15 000 neutrons interacting in each scintillator element within the central bright region. Figures 9b and 9c show reconstructed images of the source, where the pixel size is 35 $\mu$m, and the two-point resolution is about 80 $\mu$m. The neutron burn region is nearly symmetrical, with an average FWHM of 150 $\mu$m. We estimate the signal-to-noise ratio for the peak signal level to be better than 10.

In another type of experiment, we attempted to manipulate the shape of the neutron source region by altering the uniformity of laser illumination. This time, we aimed the beams to preferentially heat opposite sides of the target and to produce an extremely nonuniform drive. The reduced yield was $3.0 \times 10^{12}$ neutrons. The resulting neutron image is larger and has a more complicated shape (see Figure 10). At the 70% contour, the image is elliptical with the major axis oriented vertically, as expected; at lower contour levels, the image has several distinct lobes.

A detailed hydrodynamic computer code provides theoretical modeling of laser-fusion implosions. The computer calculations, which were carried out in one dimension and thus assume exact spherical symmetry, give neutron yields that are three to four times larger than we experimentally measure. Neutron imaging shows another discrepancy: the simulated neutron image FWHM is smaller by a factor of 15 than the experimental image (Figure 11a). The sharp peaking of the simulated neutron image is

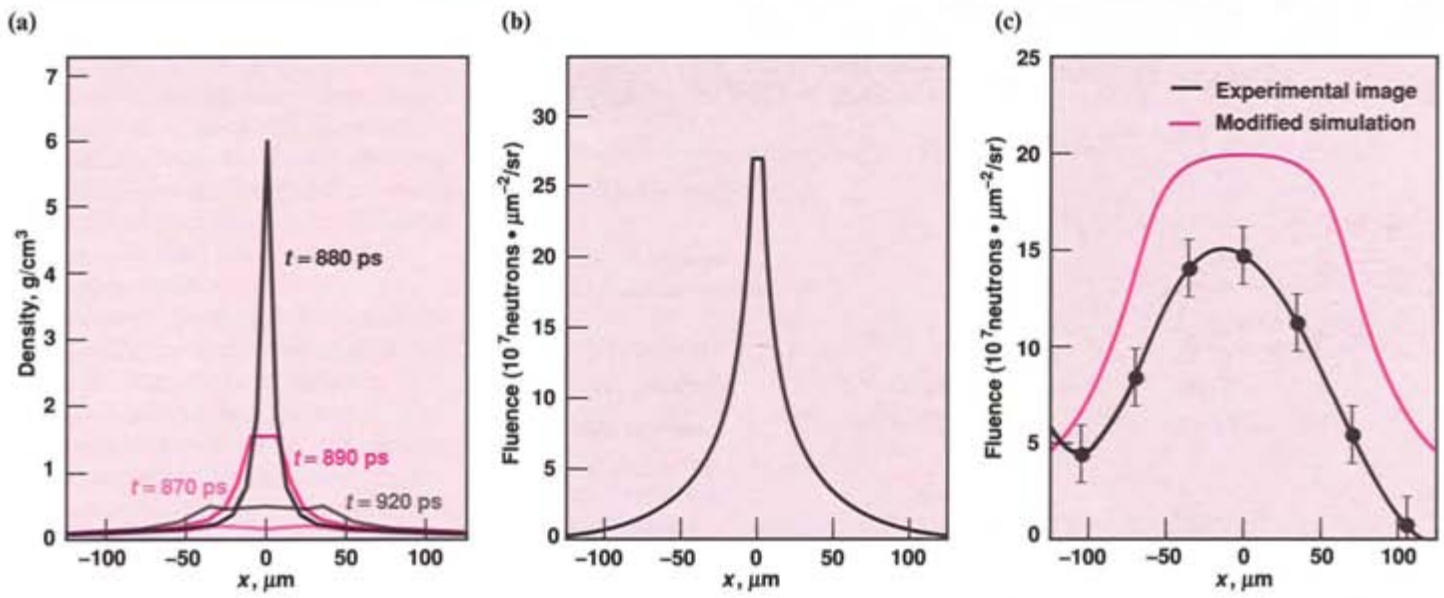


**Figure 11.** Comparison of measured neutron image with the results of a hydrodynamic computer simulation. (a) Overlay of calculated density profiles at four different times during target implosion showing the strong peaking and, thus, expected high neutron emission rate at the beginning of the D-T burn. (b) Simulated neutron image. (c) The *x*-axis lineout of the experimental image and a simulated neutron image, modified by ignoring the first 50 ps of neutron emission. By deleting the period of strong peaking of density, the calculated image now more closely agrees with our measurements.

caused by a brief, large rise in density at the center of the target (Figure 11b). This strong compression occurs during the first 50 ps of neutron emission and is associated with the final convergence of a spherical shock wave produced by the simulated laser drive. In an actual experiment, however, the laser illumination is asymmetric and may launch a strongly distorted shock front that does not converge neatly at target center, producing a lower-density compressed region that is spatially and temporally broader than the one-dimensional code prediction. This hypothesis is also supported by the neutron-emission-time measurements, which show emission time to be a factor of two to three larger than the simulation results.

Thus, two-dimensional effects appear to reduce the strong emission from the center of the target. We have illustrated this effect by producing a simulated neutron image that ignores the first 50 ps of neutron emission. The result, shown in Figure 11c, is a good match to the experiment. Moreover, the neutron yield corresponding to this portion of the burn is roughly the same as that produced by the experiment. A two-dimensional calculation is required to more accurately model our experiments.

## Summary

Information from our preliminary neutron penumbral imaging diagnostic is already providing insight into the physics of laser-fusion implosions. Our recent experiments have demonstrated the new diagnostic tool, neutron penumbral imaging. The performance of our imaging system is in good agreement with predictions based on both numerical and theoretical models. We are now improving the imaging system resolution and sensitivity through changes in the aperture and detector. During future work, we will attempt to achieve a two-point resolution better than 10 $\mu$m with enough sensitivity to allow the imaging of radiation-driven targets that achieve high radial convergence and produce neutron yields of $10^{11}$ or less. Such an enhanced imaging system is certain to become a valuable asset for future ICF research.

**Key Words:** fusion fuel—deuterium-tritium (D-T); imaging diagnostic—neutron; inertial confinement fusion (ICF); laser—Nova; neutron penumbral imaging.

**Notes and References**

1. D. T. Attwood et al., *Laser Interaction and Related Plasma Phenomena*, H. J. Schwarz et al., Eds. (Plenum Press, New York, 1981), Vol. 5, pp. 423–463.
2. K. A. Nugent and B. Luther-Davies, "Penumbral Imaging of High-Energy X Rays from Laser-Produced Plasmas," *Opt. Commun.* **49**, 393 (1984).
3. D. Ress, R. A. Lerche, R. J. Ellis, S. M. Lane, and K. A. Nugent, "Neutron Imaging of Laser Fusion Targets," *Science*, **241**, 956 (1988).
4. D. R. Kania et al., "High-Speed Detection of Thermonuclear Neutrons with Solid-State Detectors," *IEEE Trans. Nucl. Sci.* **35**, 387 (1988).